2.6 MICROSTRUCTURE, TEXTURING, MICROCRACKING AND DELAMINATION BEHAVIOR OF NFA-1 — S. Pal, M. E. Alam and G. R. Odette (UCSB), D. Hoelzer (ORNL), S. Maloy (LANL)

OBJECTIVE

The objective is to determine the origins of microcracking in 14YWT NFA-1 plate.

SUMMARY

NFA-1 was processed by gas atomization of powders, mechanical alloying by powder ball milling, consolidation by hot extrusion, annealing and hot cross-rolling. NFA-1 has highly anisotropic microstructures and mechanical properties. View planes parallel to the plate side show pancake-shaped grains of ~ 0.5 μm average thickness and aspect ratios of 2-3. Larger and a few much larger grains are also seen**.** Extrusion and cross rolling induce a strong <110> fiber texture, accompanied by brittle {001}<110> cleavage system planes parallel to the plate surface. Sessile dislocations with a Burgers vector of <001> on {001} planes along low-angle subgrain boundaries form during the the initial stages of deformation. Further deformation results in dislocation pile-ups at the subgrain boundaries, creating stress concentrations and opening displacements that nucleate microcracks on the brittle cleavage system. Microcrack propagation is driven by residual stresses that develop during the deformation.

PROGRESS AND STATUS

Introduction

Hot extruded and cross-rolled FCRD-NFA-1 is severely microcracked on planes surface of the as-processed plate [1-2]. The microcracks form during thermo-mechanical processing. This work is aimed at identifying the detailed micro-mechanisms leading to microcracking and subsequent delamination.

Experimental Methods

Microstructural characterization was carried out using SEM and TEM. EBSD was used for texture characterization. Selected region TEM lamellas were fabricated by the FIB lift out method and examined using a variety of imaging, diffraction, and micro-analytical methods.

Results

Deformation processed nano-structured ferritic (NFA-1) alloy exhibits strong anisotropy in both its mechanical properties and microstructure [1]. A significant difference in the measured values of fracture toughness and tensile strength along the thickness and longitudinal directions is observed [1-2]. The sample geometry and directions are schematically shown in Figure 1.

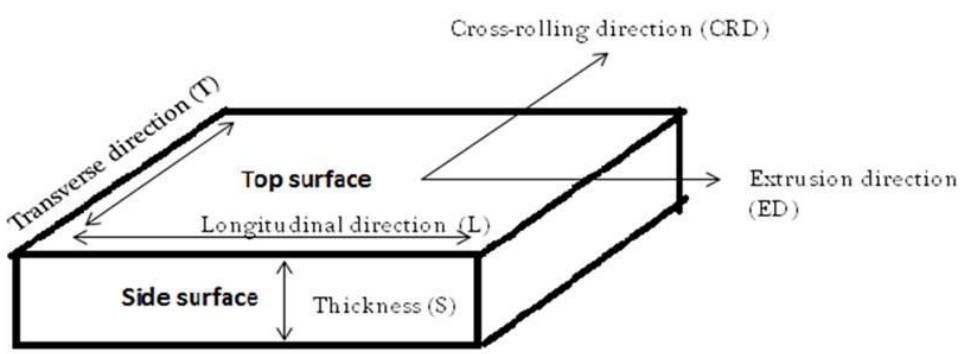

Figure 1. A schematic of the NFA-1 plate showing longitudinal (L), transverse (T) and short thickness (S) directions.

Planes parallel to the side surface is defined as LS, parallel to the top LT and parallel to the front face as TS. Extrusion and cross-rolling of the plate was carried out along the L and T direction as marked accordingly. Microstructural characterization using SEM reveals a significant difference in grain morphology and apparent sizes along the plane parallel to top surface, versus parallel to the thickness direction, as described in Figure 1. Equiaxed ~ 0.2-0.7 µm grains are observed on the plane parallel to top surface (LT view), whereas the plane parallel to thickness direction (LS view) contains elongated "pancake" shaped grains of thickness ~0.2-0.5 µm and an aspect ratio of ~ 6-7.

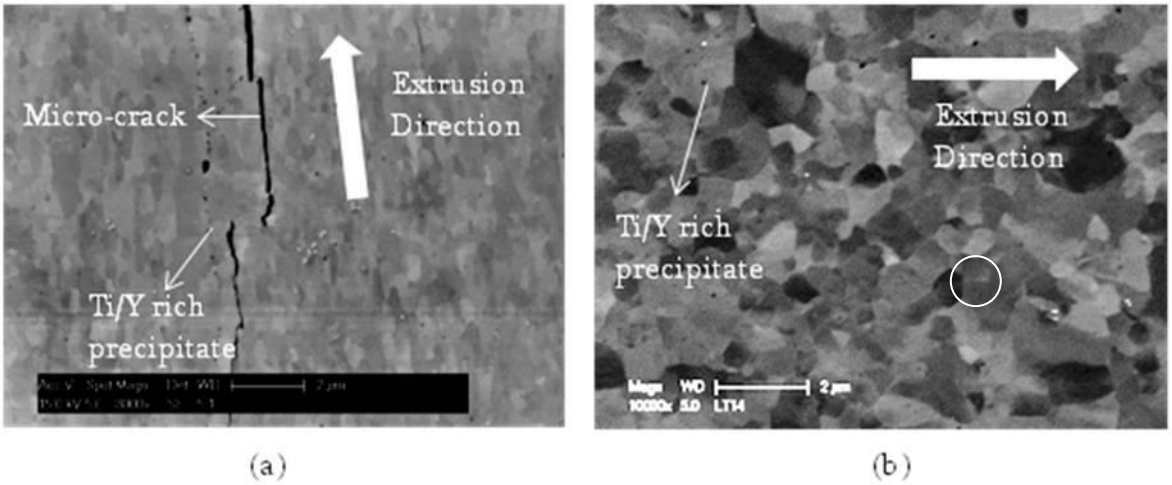

Figure 2. Polished SEM micrographs of the plate's a) LS view and b) LT view. The microstructural features (visible in the SEM micrographs) and extrusion direction for the sample are labeled accordingly.

SEM images of both the LS and LT views show the presence of Ti- and Y-rich precipitates, which are detrimental to mechanical properties. Compositional maps for both the LS view shown in Figure 3a-f and the LT view shown in Figure 4a-f were characterized using electron probe microanalysis (EPMA). The elemental composition map shown in Figure 3 and Figure 4 confirm the presence of Ti- and Y-rich precipitates in the hot extruded and cross-rolled plate. The number density of the Y-rich precipitates is lower compared to the Ti-rich features, as seen in Figure 3b and d and Figure 4b and d. The precipitates are aligned in stringers along the extrusion direction, as seen in Figure 3f and Figure 4f. EPMA maps also show that the cracked region contains oxidation peaks. Elemental maps for the LT and LS views are similar. A more detailed investigation of these Ti/Y-rich particles was carried out by TEM EDX in the high angle annular dark field (HAADF) mode as shown in Figure 5a. It was previously proposed that the microcracks might nucleate at the coarse precipitates, especially along prior powder particle boundaries. This now does not seem to be the case, since TEM clearly reveals that these features do not influence microcrack nucleation. The precipitates, which span a size range from about 15 to 150 nm and are found both in the matrix and on grain boundaries, degrade the ductility of NFA-1. The compositions of the precipitates and matrix are summarized in Table 1.

Table 1. EDX composition analysis of the Ti/Y rich precipitates and the matrix.

Feature	Composition (atom %)					
	Fe	Cr	W	Ti	Y	Cu*
Ti rich particle	2.91	1.13	-	78.94	-	16.97
Y rich particle	40.02	8.96	-	-	40.02	8.71
Matrix	78.38	14.74	0.94	-	0.28	5.22

* Cu in the EDX spectrum is due to use of a Cu grid.

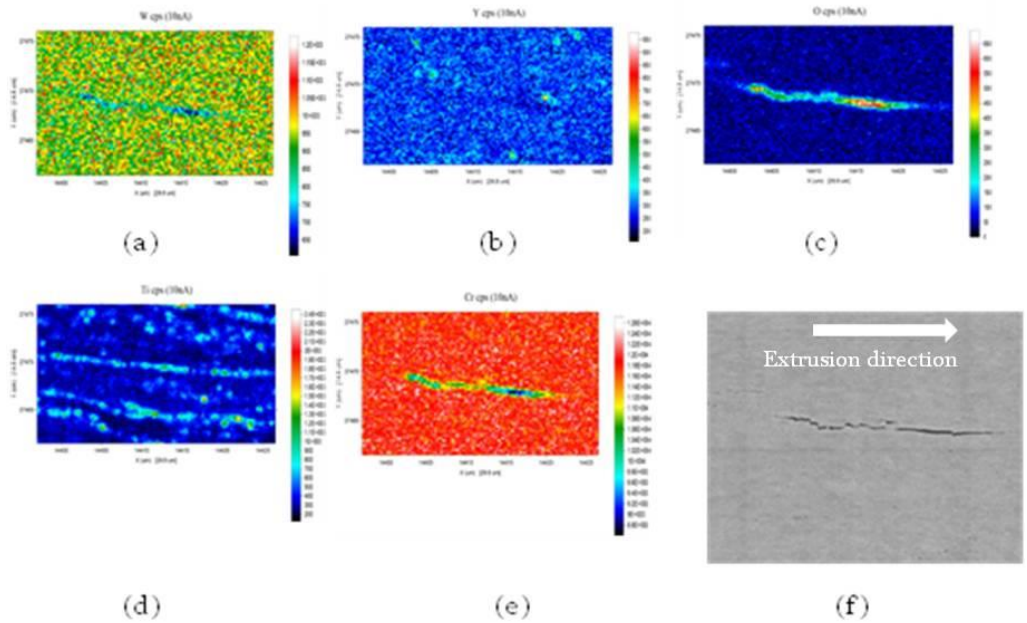

Figure 3. a-e) Elemental compositional maps for the LS view and f) the cracked region of interest.

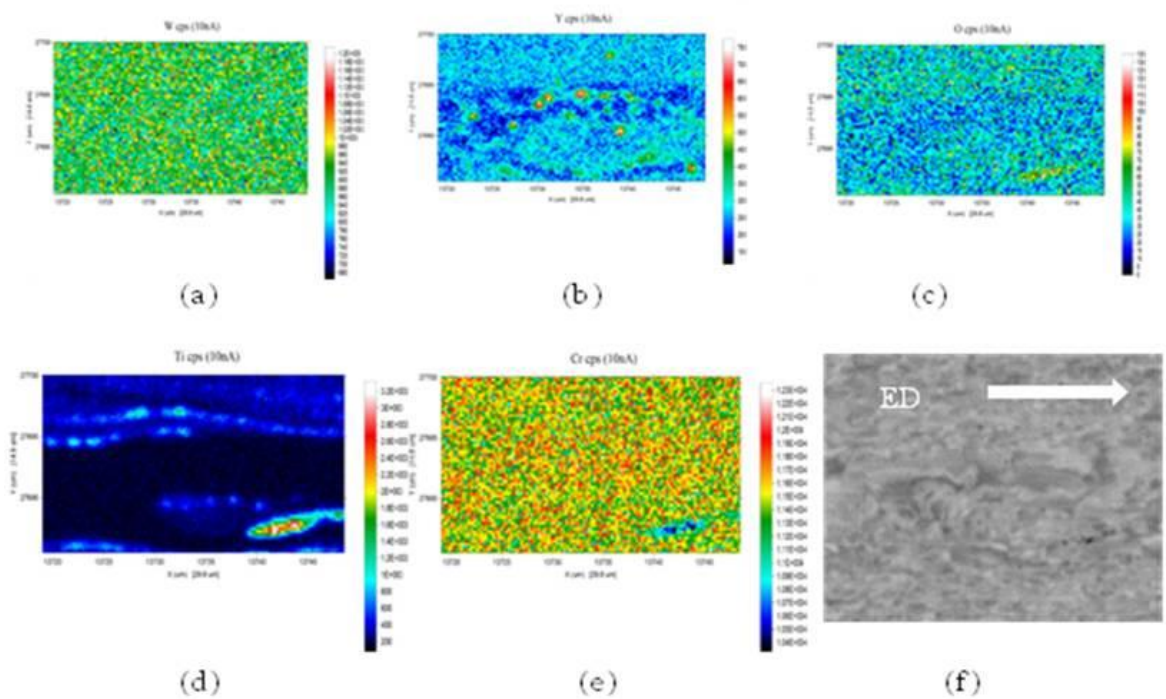

Figure 4. a-e) Elemental compositional maps of LT view and f) the cracked region of interest.

Microcracks are observed only in the plate side SL view, running throughout the plate thickness (S). Similar microcracking has been previously reported in the literature [3-4]. The microcrack size, number density, inter-crack spacing, and opening dimensions are summarized in Table 2. The microcracks play a very critical role in determining the fracture toughness of NFA-1, especially by nucleating delaminations

that relax the triaxial stress state towards a plane strain condition, thereby lowering internal stresses and suppressing cleavage; alternately, delaminations cause crack deflections for LS orientations. However, microcracks reduce the tensile ductility and strength in the thickness (S) direction [1].

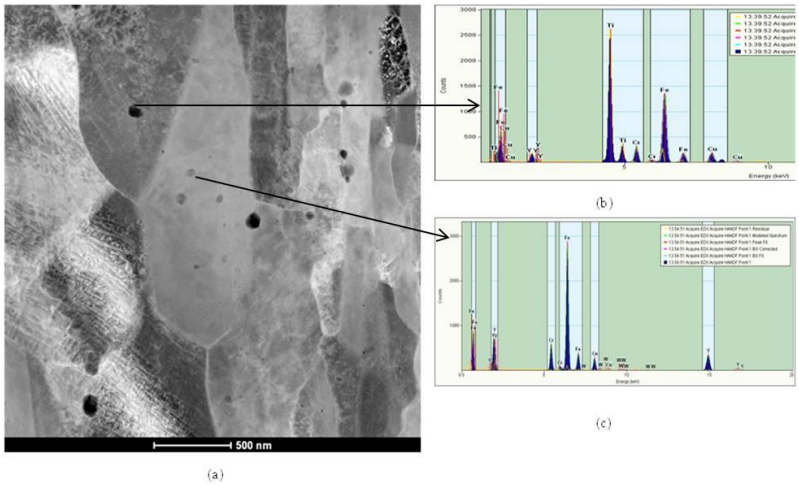

Figure 5. a) HAADF image showing Ti/Y-rich precipitates with darker contrast; b) EDX spectrum of the Ti rich precipitates; and c) EDX spectrum for the Y rich precipitates.

Table 2. Microcrack Statistics

Item	Number	Standard Deviation
Average crack separation (µm)	~ 16.3	± 4.7
Crack length (µm)	~ 10.2	± 8.9
Number density (/m^2)	~ 3.45×10^9	± 1.2×10^9
Crack mouth opening displacement (nm)	~ 252	± 142

Texture characterization

Figure 6 shows the directions and planes that are used to define texturing with respect to the primary deformation orientations. Texture measurements for different views of the plate planes were first carried out by pole figure (PF) analysis. Projections of two major deformation axes, along with the plate normal direction, are shown in stereogram in Figure 6b and c for both the LT and LS views, respectively.

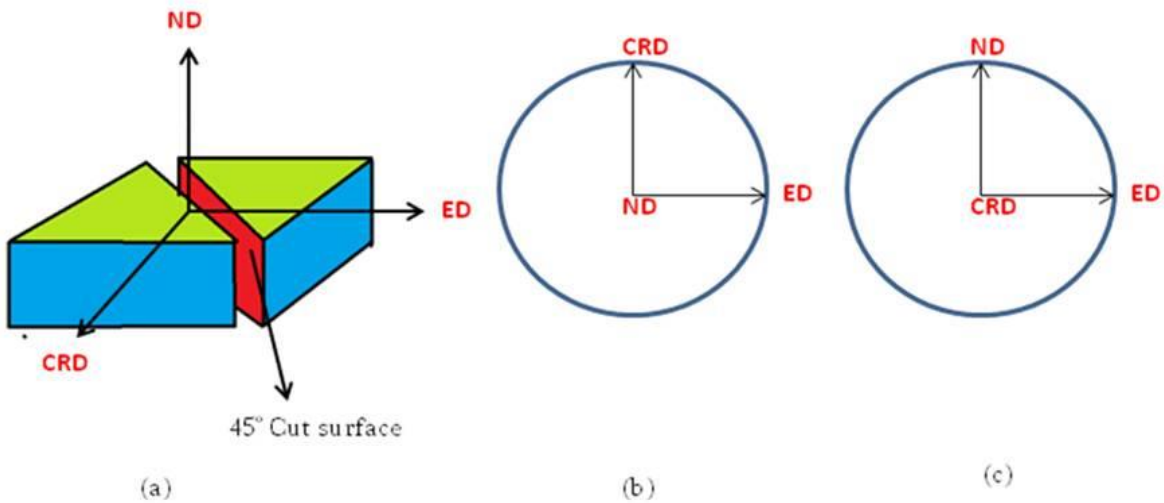

Figure 6. a) A schematic representation of the plate along with primary deformation axes of extrusion (ED), cross-rolling (CRD) and normal direction to the plate (ND). b) and c) Stereogram equivalent deformation axis directions for the LT and LS views, respectively.

EBSD PF maps in in Figure 7a show that the plate has an expected strong α-fiber texture (<110>) along the extrusion direction. Figure 7b shows that a partial α-fiber also develops along the cross-rolling direction. This suggests that both the primary deformation processes (hot extrusion and cross-rolling) induce a similar type of <110>-fiber texture. PF analysis also shows that the texture component developed along the surface normal direction is <001>. EBSD characterization of surface cuts at 45° with respect to the extrusion direction (as illustrated in Figure 6a) in Figure 8 also show that the texture for the LT plate surface normal is predominantly <100>. The PF analysis in Figure 8 also shows that the planes parallel to the 45° cut surface are {100}-type. These observations are further corroborated by the inverse pole figure (IPF) analysis in Figure 9.

More quantitative and accurate determination of the texture components was carried out based on an orientation distribution function (ODF) analysis. The Φ_2 = 0 and 45° ODF sections, shown in Figure 9a and b, demonstrate that a strong {001}<110> texture is dominant in the plate. This is also the low-toughness cleavage system in bcc Fe.

Taken together, the most important conclusion is that a strong {001}<110> texture system develops in the thickness direction of the extruded and cross-rolled plate.

Characterization of crack propagation and initiation by TEM

A brittle crack is characterized by its direction and plane of propagation. TEM was used to characterize the propagation plane-direction and the microcrack formation mechanism. TEM lamellas in Figure 11b and d, taken from locations shown in Figure 11a and c, were prepared using FIB lift-out method. The largest separation between the crack surfaces indicates the crack initiation site.

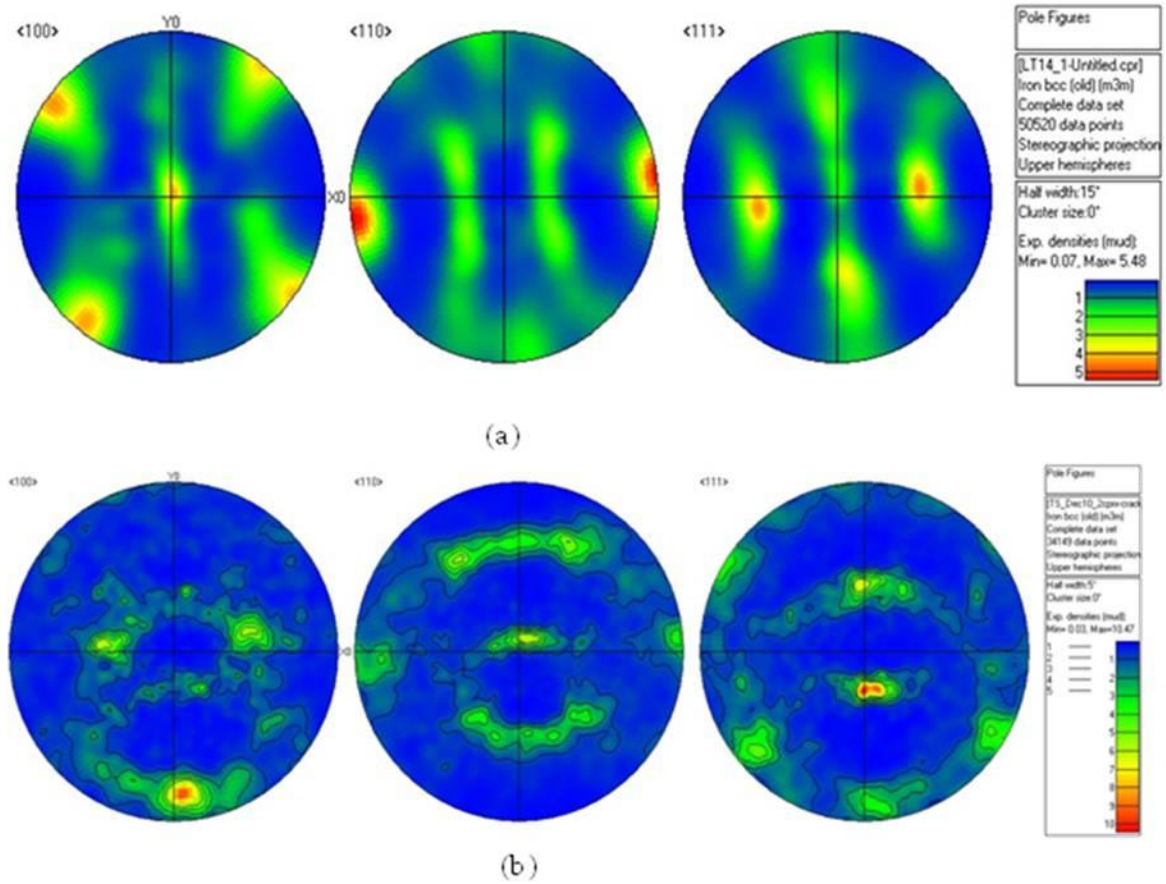

Figure 7. Pole figures of a) LT view and b) LS view of the as-extruded plate showing projection of <100>, <110>, and <111> poles.

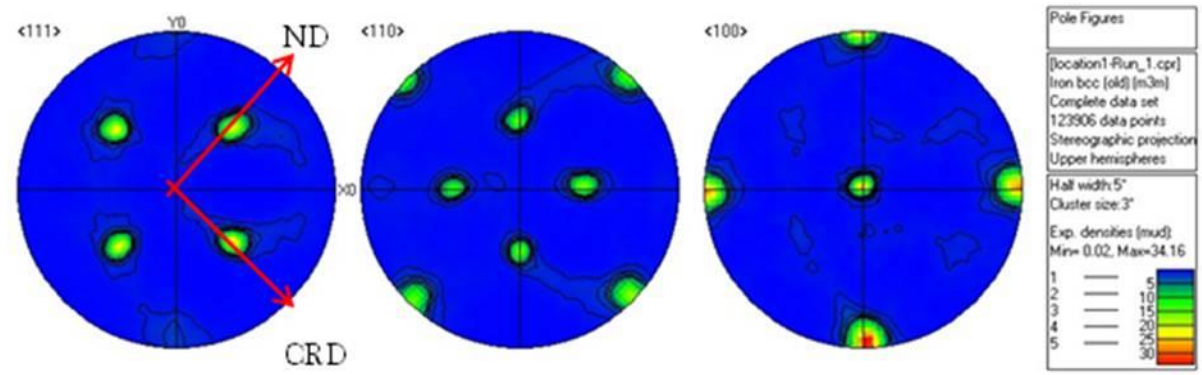

Figure 8. PF for the 45° cut surfaces showing <111>, <110>, and <100> projections. Red arrows indicate the deformation directions of the plate for the <111> projection.

.

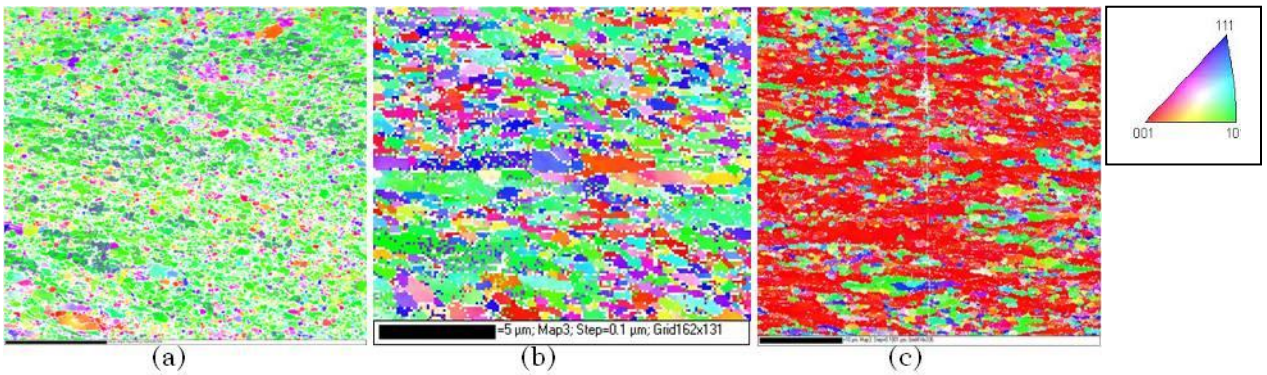

Figure 9. IPF maps of a) LT, b) TS, and c) 45° cut section showing density of the planes parallel to the surface of respective samples.

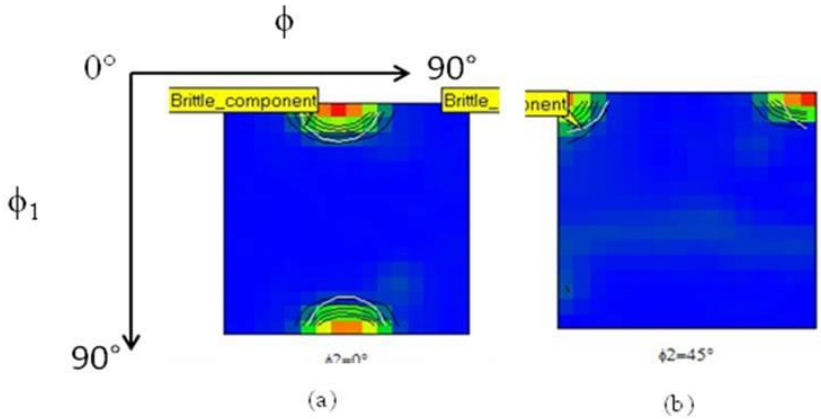

Figure 10. a) Φ_2 = 0 and b) Φ_2 =45° ODF sections of the plate.

Figure 11 shows the FIB locations where TEM lamella were extracted along both the propagated crack front and initiation site. Figure 12a is a bright field (BF) TEM image of the propagation front lamella shown in Figure 11b. The crack runs through a single grain with a contrast variation due to a high dislocation density and a low-angle boundary. Selected area diffraction (SAD) patterns for the marked locations in Figure 12a, along with dark field (DF) imaging, confirm that the crack is confined to a single (001) oriented grain. The SAD patterns from the near crack tip locations, marked as 1 and 2 in Figure 12a, show that the foil normals are near <110>, and are only slightly misoriented with respect to each other. The weak beam dark field (WBDF) image in Figure 12b uses the (002) reflection, marked by the dashed circle in Figure 12c, in the g-3g condition. Dislocations, seen as the bright contrast in Figure 12b, are concentrated around the crack and low-angle boundary.

A BF image of the propagating crack region is shown in Figure 13a. The WBDF in Figure 13b, and the HAADF image in Figure 13c, also show dislocation pile-ups in the vicinity of a crack. Further, Figure 13 suggests that a low-angle subgrain boundary is formed in a grain by the accumulation of dislocations. Contrast in HAADF images is sensitive to variations in mass-thickness and local strain fields. Since the FIB lamella thickness is nearly uniform, the contrast variation in the Figure 13c can be largely ascribed to corresponding variations in the local strain fields. Eight TEM lamellas were prepared from the crack initiation regions and illustrative BF and DF images are shown in Figure 14a and c. along with the corresponding SAD patterns in Figure 14b. Clearly, the microcrack nucleates on a {100}-type plane and propagates in a transgranular mode.

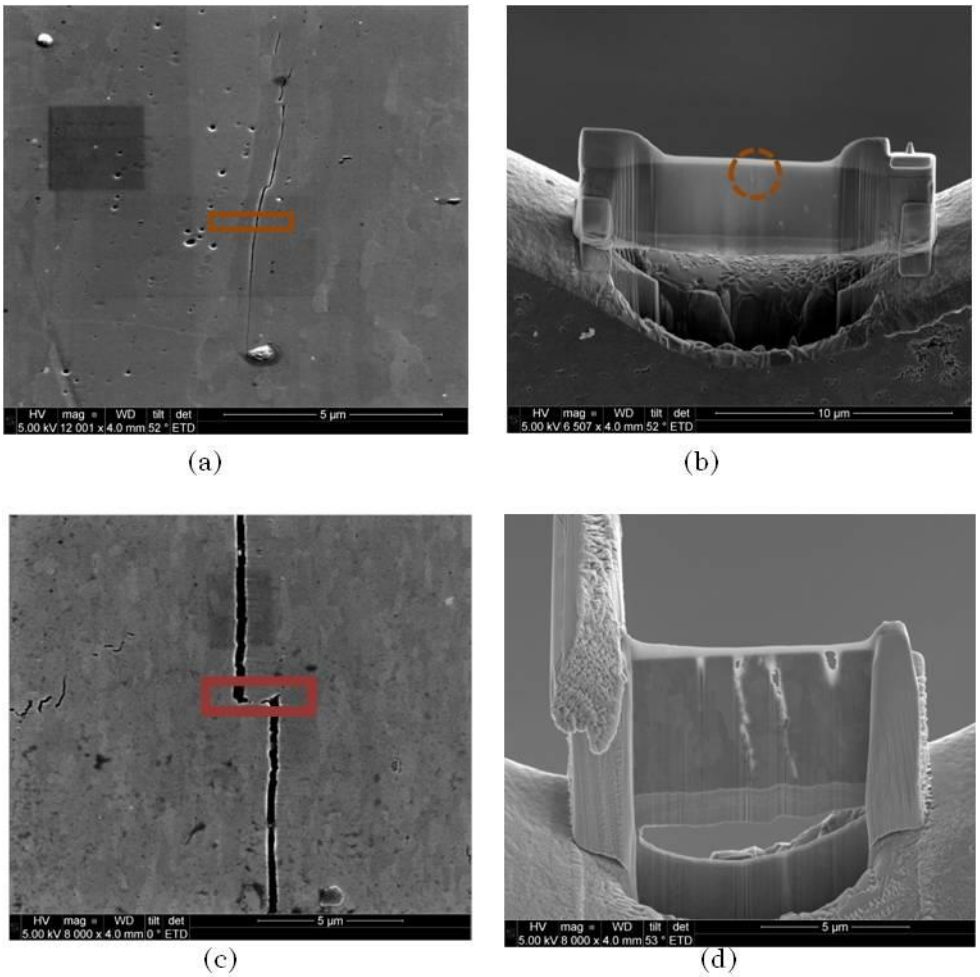

Figure 11. a) The marked location where the TEM lamella was extracted to characterize the crack propagation front; b) the corresponding FIBed lamella; c) the marked location crack initiation front where the TEM lamella was extracted; and d) the corresponding FIBed lamella.

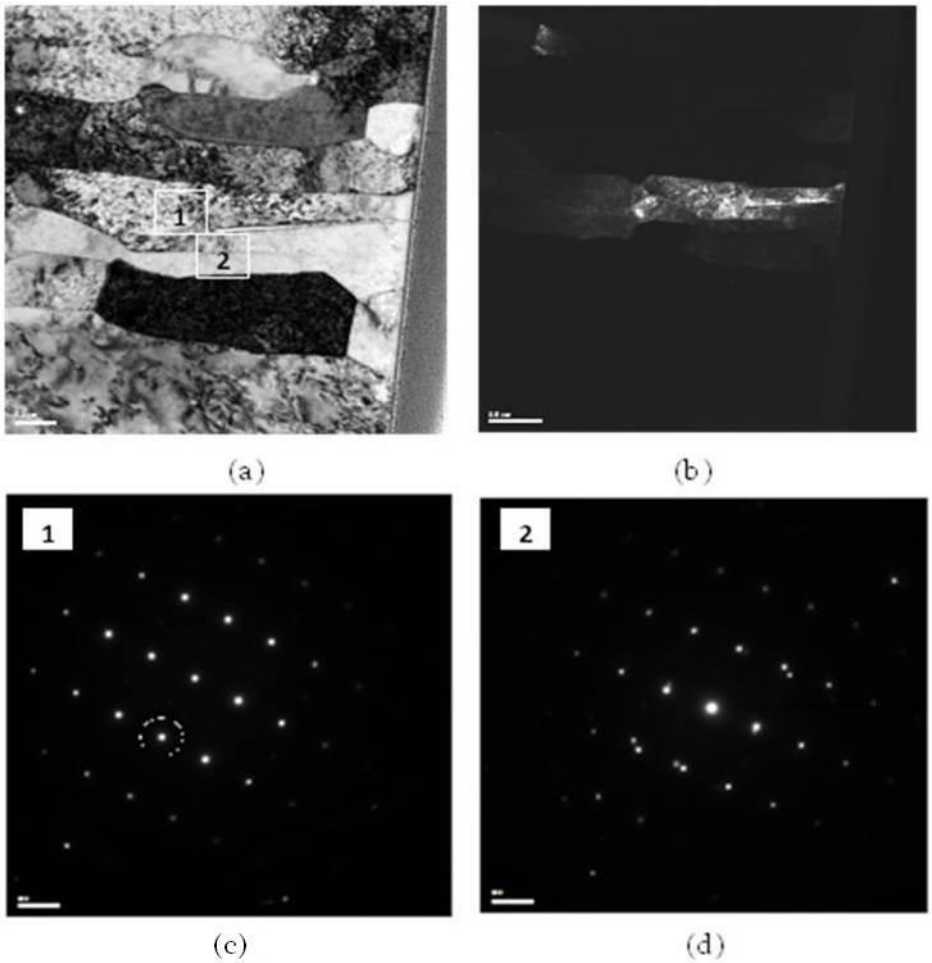

Figure 12. a) BF image, b) WBDF image using the (002) reflection marked in Figure 12c, and c-d) SAD patterns for the marked locations in Figure 12a.

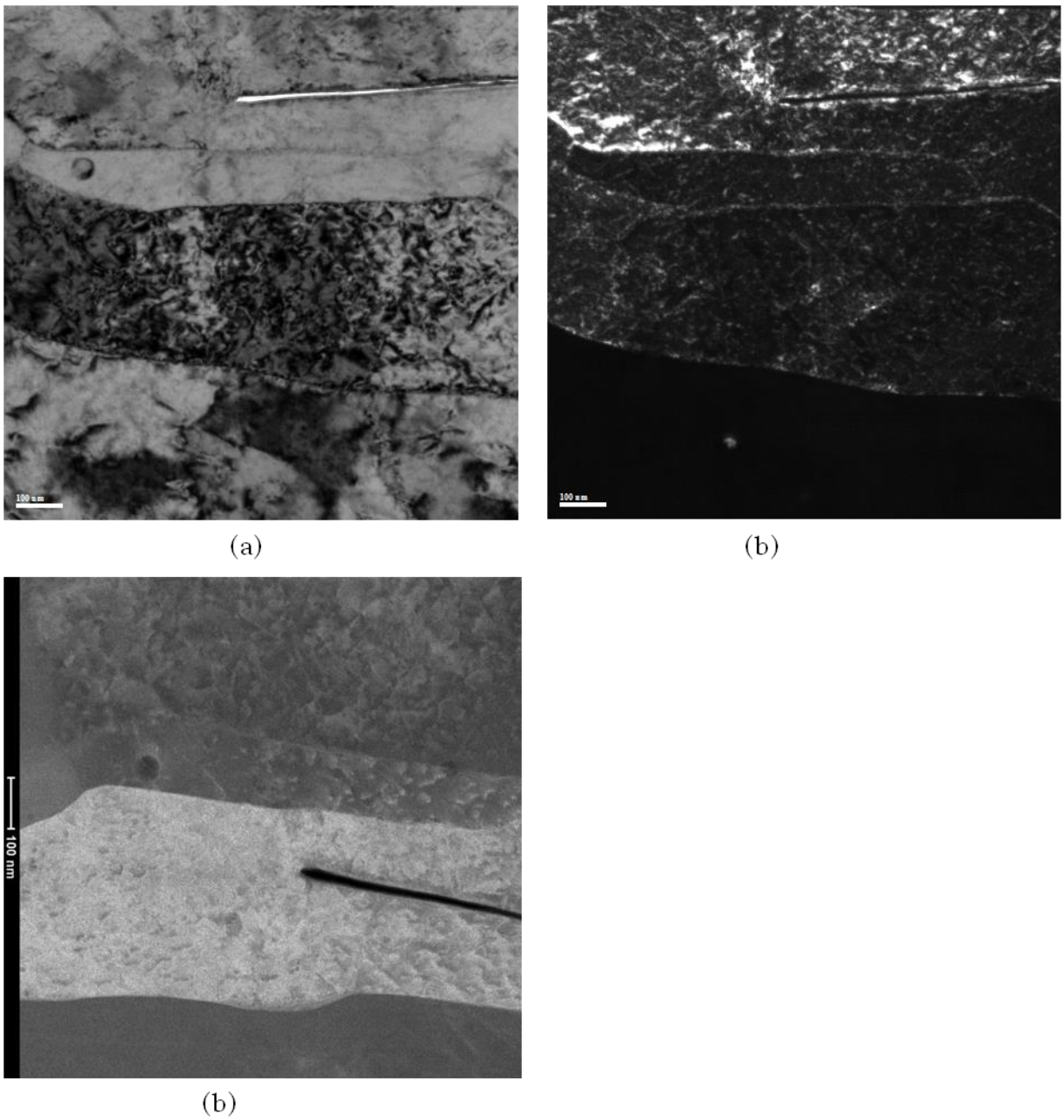

Figure 13. a) BF, b) WBDF, and c) HAADF images of the crack propagation plane.

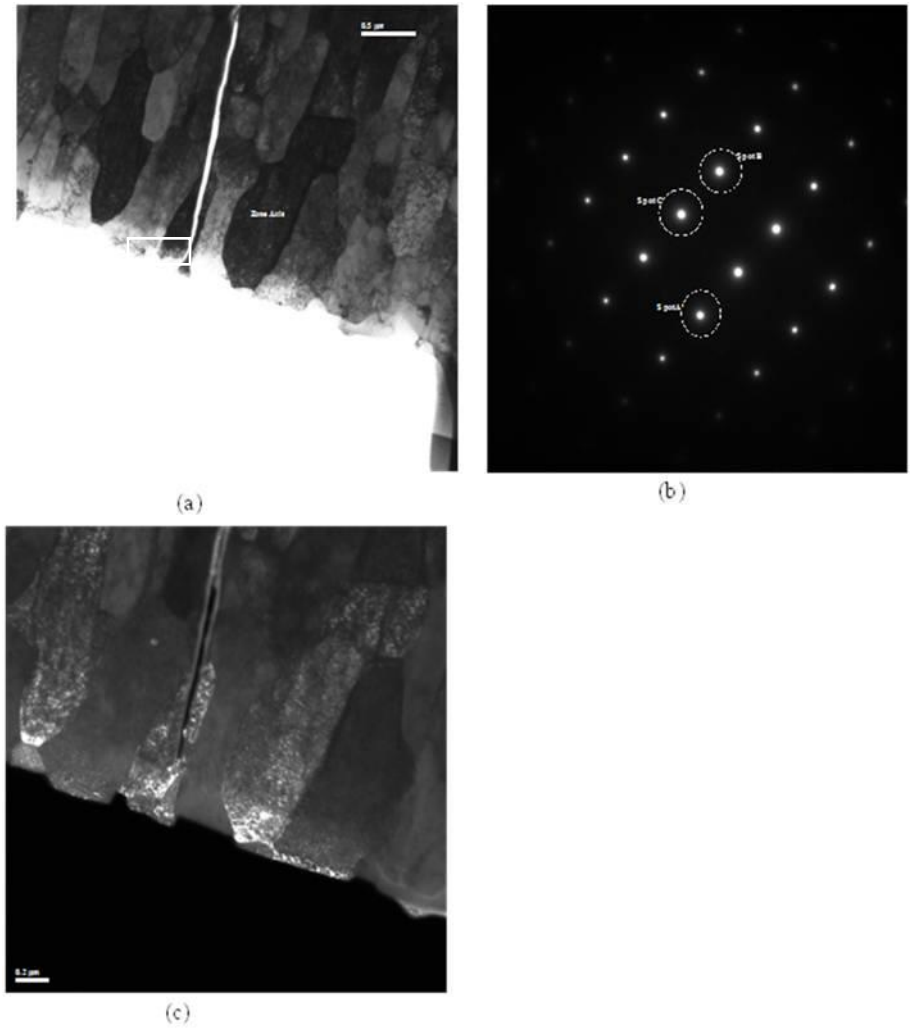

Figure 14. a) BF image of the crack initiation front. Marked grain is tilted to the zone axis conditions. b) SAD pattern of <110> zone axis captured from the grain marked using white box in Figure 14a. c) DF image captured from the (002) spot labeled in Figure 14b.

The higher-magnification view of the crack region in Figure 15 shows very diffuse boundary-like contrast parallel to the crack. Dislocation tangles are clearly seen inside the grain in Figure 15a and b. Figure 15b shows that cracks propagate along the subgrain boundary, which originated from dislocation a pile-up.

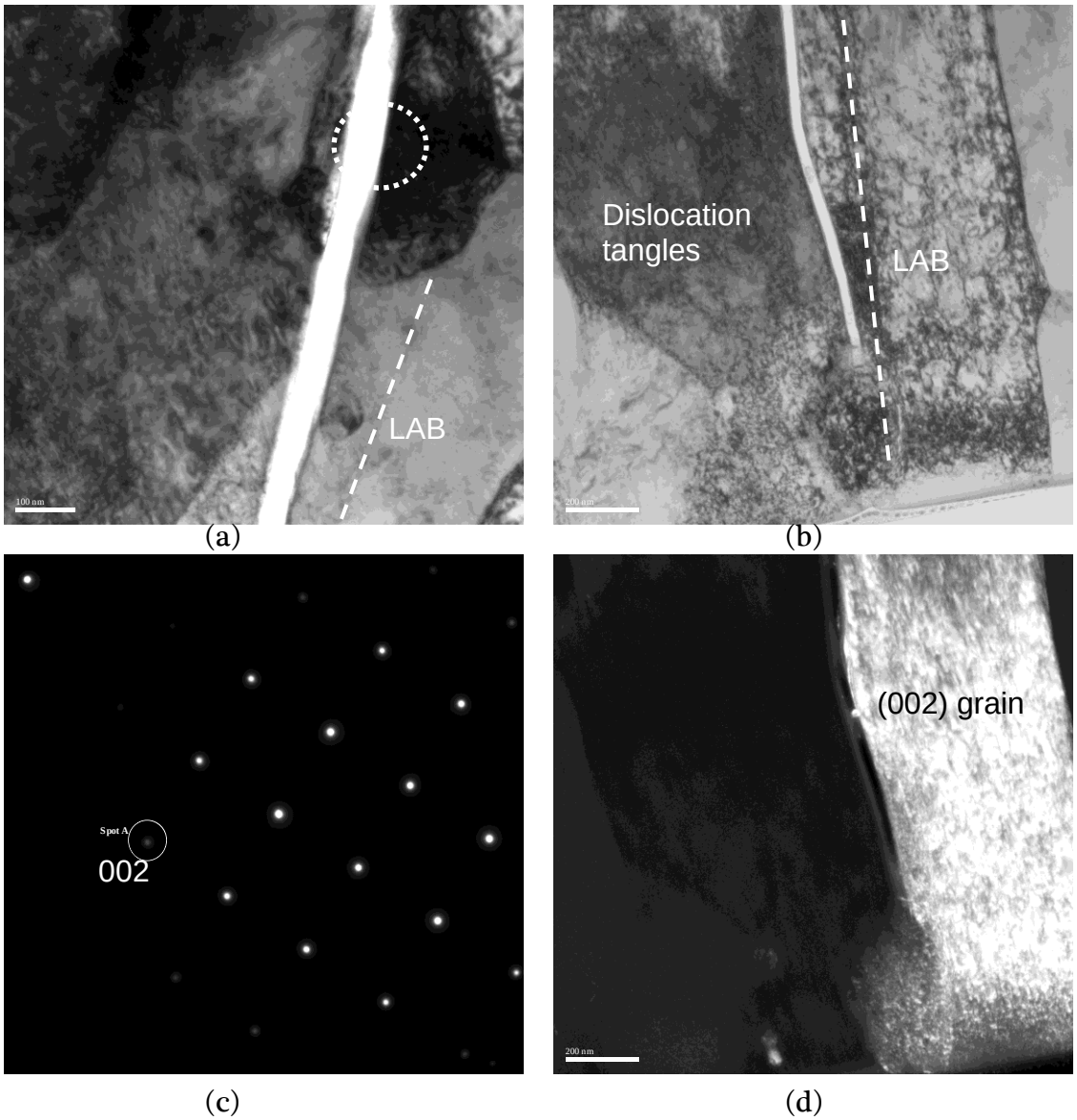

Figure 15. a) BF image of a cracked region showing low-angle boundary (LAB) in a grain; b) BF image of the same location under different tilting conditions; c) SAD pattern from the marked region in Figure 15a showing the grain orientation <110>; and d) DF image corresponding to the (002) reflection of the SAD pattern shown in Figure 15c.

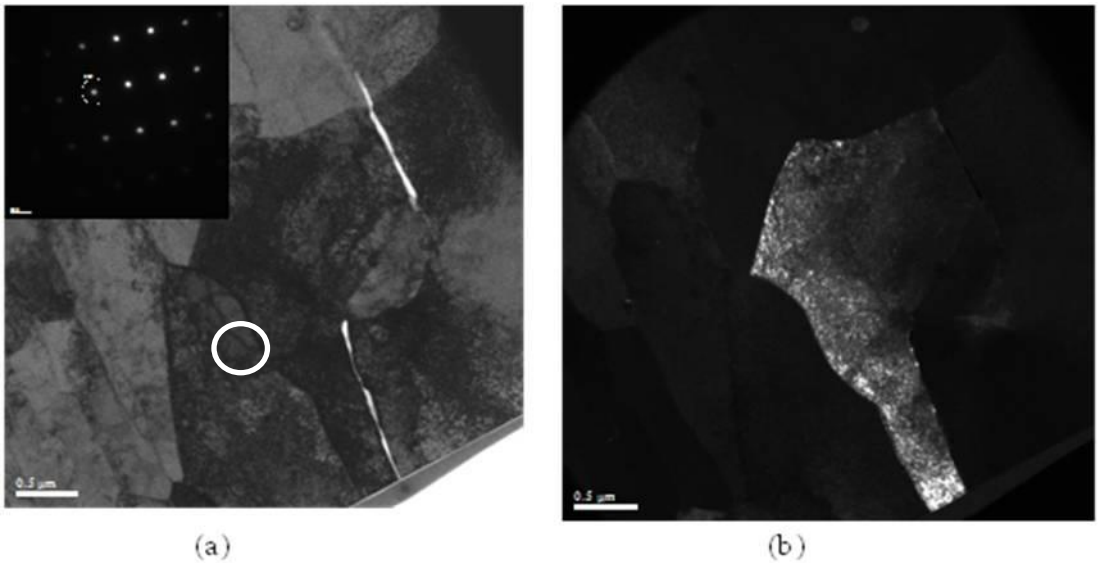

Figure 16. a) BF image of the cracked region, where the insert shows the SAD pattern for the (110) zone axis at the marked location; and b) DF image corresponding to the (002) reflection in the inset SAD pattern of Figure 16a.

Figure 16 and Figure 17 lend additional support to our hypothesis regarding the nucleation of microcracks associated with dislocation pile-up at low-angle subgrain boundaries. Figure 16 again shows that crack originates on a {001} plane in a grain that contains a high density of dislocations. The SAD patterns shown in Figure 17 for different locations near the crack, as marked by red circles in the BF image, show that all the SAD patterns belong to a nearly common zone axis with only minor deviations from <110>. These results clearly demonstrate that cracks are formed in association with low-angle grain boundaries by dislocation pile-ups. All the microstructural components are contained in the HAADF image in Figure 18, taken from the same locations seen in Figure 16a and Figure 17. The HAADF micrograph clearly shows the low-angle boundary parallel to the crack and that the dislocation pile-ups develop the boundary.

Thus we hypothesize that the sequence of events leading to microcracking is as follows: a) the initial deformation is accommodated by formation of low-angle dislocation subgrain boundaries; b) further deformation creates dislocation pile-ups at these low-angle subgrain boundaries; c) the local stress concentrations and accumulated opening displacements nucleate microcracks on {100}-type planes; d) once nucleated, the microcracks propagate transgranularly along the low-angle subgrain boundaries on {100}-type cleavage planes.

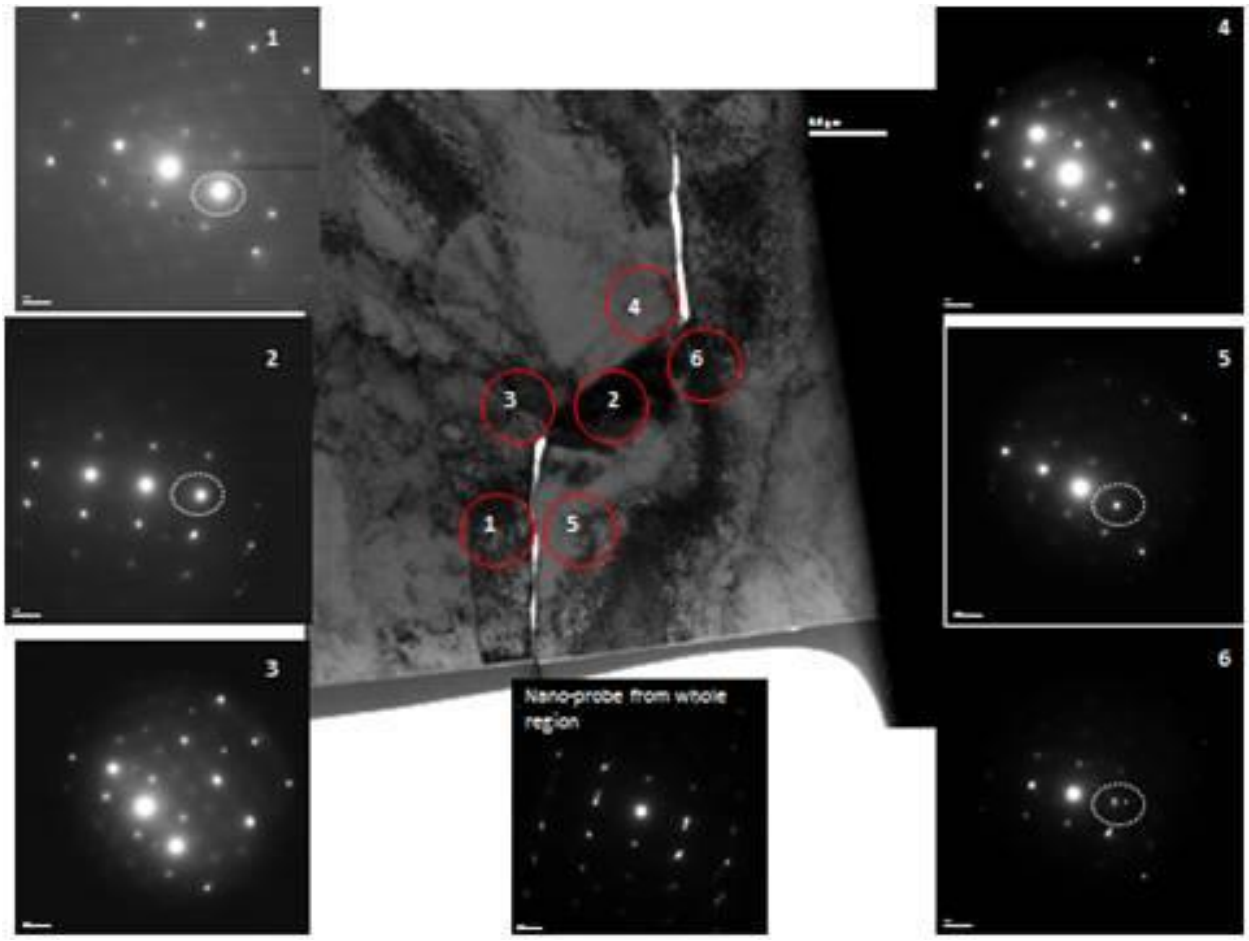

Figure 17. SAD patterns and their corresponding locations in the same cracked region as shown in Figure 16. The misorientations between all the patterns are very low.

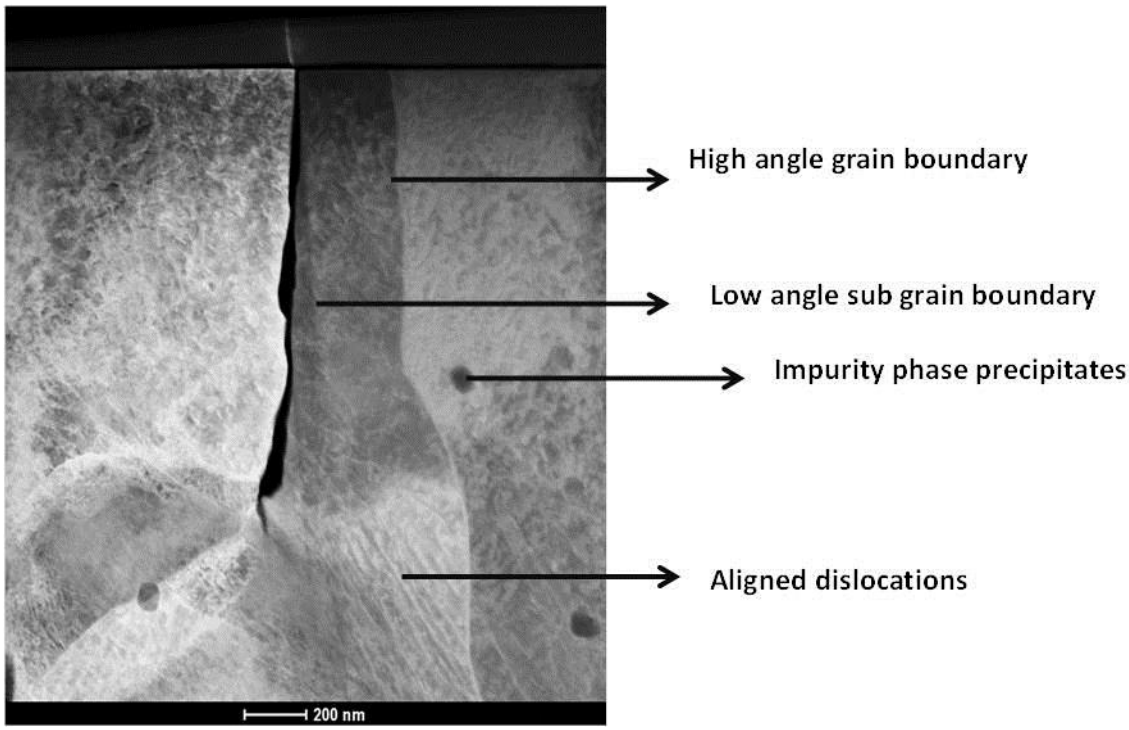

Figure 18. HAADF image of the crack front showing different microstructural components.

Summary and Discussion

Microcracking and delamination in pipeline steels are well-established phenomena. Various reasons for this behavior have been proposed, including: inter-phase boundary fracture, the presence of carbide and inclusion particles, texture, banding, and anisotropic plastic deformation [3-4]. Unfortunately a clear responsible micro-mechanism operating during thermo-mechanical processing and texture development is not in hand. Most of these reported results are for dual-phase steels containing combinations of ferrite/austenite/martensite constituent grains and their biphasic interfaces [3-4]. In the present investigation, microcracking and delamination occur in a fully ferritic steel (14YWT NFA-1). The extruded and cross-rolled NFA-1 plate exhibits a strong α-fiber texture (<110>∥ ED). ODF analysis coupled with IPF mapping shows that presence of a {001}<110>-texture component in planes normal to the short, plate thickness direction. This is the most brittle cleavage system in bcc Fe. TEM clearly shows that cracks nucleate and propagate on {100}-type planes and run along low-angle subgrain boundaries parallel to {100} in the <110> direction. Since {110} are the easy glide planes in bcc structures, grains containing these planes become elongated along the extrusion direction. In contrast, glide is difficult on {100}-type planes. Under sufficiently high stress, two a/2[111] + a/2[-1-11] dislocations react on a {001} plane to form a sessile [001] dislocation [5]. Subsequent dislocation pile-ups create stress concentrations and opening displacements that nucleate a microcrack. The fracture toughness for the {001} <110> cleavage system is extremely low, of order ~ 5-10 MPa√m. This microcrack growth is further driven by the residual stresses that develop during the thermo-mechanical processing.

The existence of residual stress is supported by streaking in the SAD patterns in Figure 19b collected from different locations near the cracks within a single grain marked in Figure 19a. These SAD patterns are taken along the <111> zone axis of bcc Fe. Streaking of the diffraction spots usually could be attributed to residual stress that generates strain even within a single grain. Initially the deformation is accommodated through low-angle subgrain boundary formation on {001} planes by creating sessile <001> dislocations that form subgrain boundaries. These subgrain boundaries are also aligned along the primary deformation direction. Further deformation causes dislocation pile-ups and produces crack

opening displacements. These cracks propagate on the brittle cleavage system {001}<110> aligned along the subgrain boundaries.

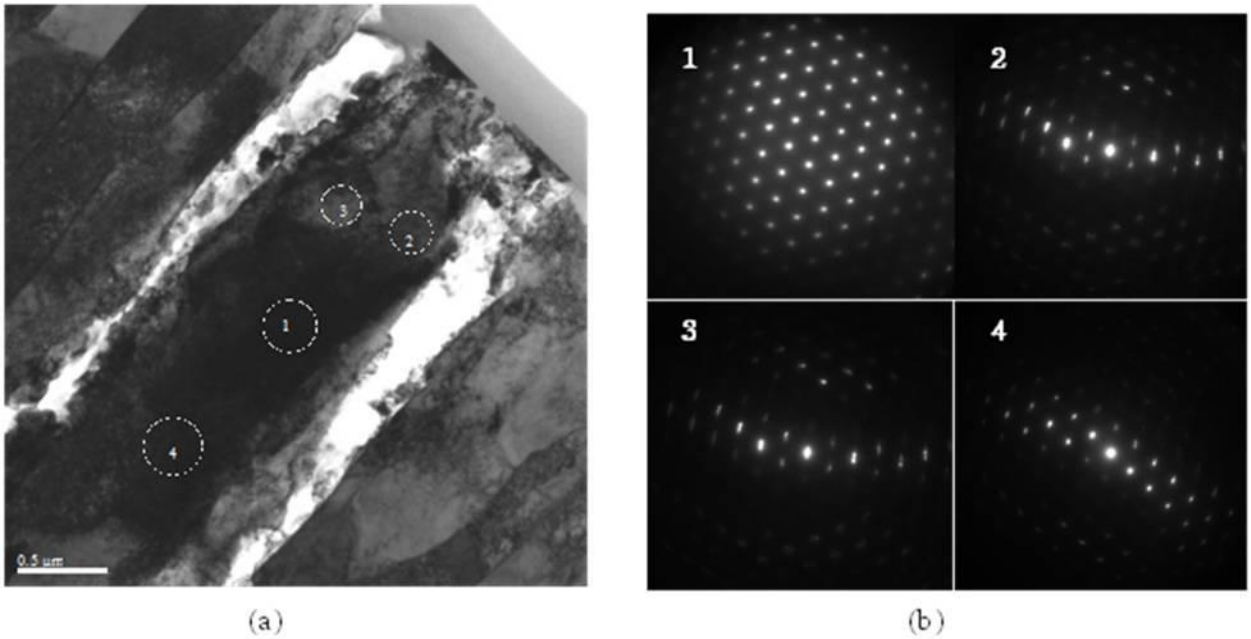

Figure 19. a) BF image of the cracked regions and (b) streaked SAD patterns from the locations marked in the BF image.

Conclusions

- Thermo-mechanical processing of the NFA-1 alloy produces a microstructure containing a tri-modal distribution of small (< 1 μm), medium (1 – 10 μm) and large grains. The pancake-shaped grains are compressed in the plate reduced-thickness direction and elongated in the cross-rolling and especially extrusion directions, with and average aspect ratio ranging from 2-3 when viewed along a side LS view surface.

- NFA-1 contains coarser Ti- or Y-rich precipitates/inclusions in the size range of ~ 15-150 nm. However, these features do not appear to affect microcracking.

- Microcracking of as-processed NFA-1 alloy is related to texture development during deformation processing. The plate develops α-fiber texture along the extrusion and cross-rolling directions, which results in alignment of the {001}<110> brittle cleavage plane-direction system normal to the plate thickness direction.

- Initial deformation is accommodated by a/2[110] dislocation glide. Dislocations react to form low-angle subgrain boundaries composed of sessile a[001]-type dislocations on {001} planes. Further deformation leads to additional dislocation pile-ups at the subgrain boundaries that create stress concentrations and opening displacements, which nucleate a cleavage microcrack. Transgranular cleavage microcrack propagation occurs on the {001} <110>-cleavage system and is further driven by residual stresses that develop during deformation processing.

References

[1] G.R. Odette, “Recent progress in developing and qualifying nanostructured ferritic alloys for advance fission and fusion applications” JOM, 66-12 (2014) 2427.

[2] M. E. Alam, N. J. Cunningham, D. Gragg et al., **"**Mechanical property characterization of a larger best practice heat of 14YWT NFA1**"**, DOE/ER-0313/56 (63-69)

[3] H.C.Chao, "Mechanism of anisotropic lammellar fractures", Met. Trans. A, 9A (1978) 509.

[4] D. L. Bourell and O. D. Sherby "Texture induced cleavage delamination of warm-rolled low carbon steel", Met. Trans. A, 14A (1983) 2563.

[5] A.H. Cottrell, "Theory of brittle fracture in steel and similar metals**",** Trans. A.M.I.E, 212 (1958), 192-203.